



Full length article

Modulation of plastic flow in metallic glasses via nanoscale networks of chemical heterogeneities



Jinwoo Kim ^a, Hyun Seok Oh ^a, Wan Kim ^a, Pyuck-Pa Choi ^b, Dierk Raabe ^c, Eun Soo Park ^{a, *}

^a Research Institute of Advanced Materials, Department of Materials Science and Engineering, Seoul National University, Seoul, 08826, Republic of Korea

^b Department of Materials Science and Engineering, Korea Advanced Institute of Science and Technology, 34141, Daejeon, Republic of Korea

^c Max-Planck-Institut für Eisenforschung, Max-Planck-Str. 1, 40237, Düsseldorf, Germany

ARTICLE INFO

Article history:

Received 21 April 2017

Received in revised form

10 July 2017

Accepted 2 August 2017

Available online 11 August 2017

Keywords:

Metallic glass

Metastable miscibility gap

Chemical heterogeneity

Shear avalanche

Plasticity

ABSTRACT

We systematically investigate the microstructures of metallic glasses with nanoscale networks of chemical heterogeneities introduced by the presence of a metastable miscibility gap, and their effects on modulating plastic flow of the alloys. Microstructural analysis of as-quenched alloys and the associated thermodynamic assessment in Cu-Zr-Al-Y metallic glass-forming system suggest that the existence of a metastable miscibility gap can induce not only phase-separated microstructures with sharp phase interfaces but also compositional fluctuations without a clear interface ranging from atomic scale to a few-nanometer scale in the fully amorphous alloys. The statistical analysis of shear avalanches in such compositionally heterogeneous metallic glasses reveals that chemical heterogeneities extending over a few nanometers promote a relatively large population of shear deformation units jammed before the nucleation of mature shear bands. This leads to the multiple nucleation of shear bands and sluggish deformation behavior along them. However, phase interfaces formed by phase separation inside the miscibility gap promote rapid propagation of shear bands at low flow stress, while compositional fluctuations creating non-sharp interfaces emerging at the outside of miscibility gap have relatively high resistance against shear band propagation. We hence suggest that the optimization of nanoscale compositional fluctuations in metallic glasses in terms of topology, percolation and magnitude can be an effective route for improving the materials' damage tolerance upon plastic flow.

© 2017 Acta Materialia Inc. Published by Elsevier Ltd. All rights reserved.

1. Introduction

The limited room-temperature plasticity of metallic glasses has been a crucial shortcoming for their use in structural applications, despite their superior mechanical properties before yielding such as high strength and large elastic strain limit arising from the absence of compositional and structural long-range order [1]. The brittle fracture of metallic glasses originates in an abrupt and catastrophic propagation of a small set of shear bands accompanied by highly localized stresses and a lack of intrinsic crack propagation barriers such as grain boundaries [2–4]. Turning the shear banding behavior from a highly localized and inhomogeneous mode towards a more distributed and dissipative pattern has been a significant issue for enhancing ductility of metallic glasses. In this regard, various composite structures composed of a metallic glass

matrix and nano-to micrometer scale crystalline secondary phases have been reported to successfully inhibit the rapid propagation of shear bands and impart pronounced ductility and toughness to the alloys [5–9].

However, for monolithic metallic glasses, atomic-scale structural manipulation can also improve their plasticity via thermo-mechanical processing [10] or minor addition of alloying elements [11]. The former measure controls the effective cooling rate of metallic glasses through post-processing such as thermal cycling [12], elastostatic loading [13,14] and severe plastic deformation [15,16], and renders the atomic structure of the alloys into a rejuvenated state [10]. The introduction of widely-distributed 'soft spots' [17] in an amorphous matrix via the structural rejuvenation enables the improvement of mechanical stability [10]. On the other hand, the minor addition of alloying elements, especially those with a positive enthalpy of mixing relation with the major alloying elements, induces atomic scale heterogeneities [18] in as-cast monolithic bulk metallic glasses. Chemical heterogeneities featuring at small size scale under a few nanometers affect the flow

* Corresponding author.

E-mail address: espark@snu.ac.kr (E.S. Park).

characteristics of local regions under shear deformation. This results in improved plasticity which was revealed for various bulk metallic glasses with optimized compositions such as $\text{Cu}_{46}\text{Zr}_{47}\text{Al}_7(\text{Y,Gd})_5$ [18,19] ($\Delta H_{\text{Zr-(Y,Gd)}}^{\text{mix}} = +9$ kJ/mol), $\text{Zr}_{57}\text{Ta}_5\text{Cu}_{18}\text{Ni}_8\text{Al}_{10}$ [20] ($\Delta H_{\text{Zr-Ta}}^{\text{mix}} = +3$ kJ/mol), $\text{Ni}_{59}\text{Zr}_{16}\text{Ti}_{13}\text{Si}_3\text{Sn}_2\text{Nb}_7$ [21], $\text{Cu}_{47}\text{Ti}_{33}\text{Zr}_7\text{Nb}_4\text{Ni}_8\text{Si}_1$ [22] ($\Delta H_{\text{Zr-Nb}}^{\text{mix}} = +4$ kJ/mol, $\Delta H_{\text{Nb-Ti}}^{\text{mix}} = +4$ kJ/mol) and $\text{Cu}_{55}\text{Zr}_{30}\text{Ti}_{10}\text{Ag}_5$ [23] ($\Delta H_{\text{Cu-Ag}}^{\text{mix}} = +2$ kJ/mol) (we refer to [24] for the values of ΔH^{mix}). Both approaches to enhance the plasticity of monolithic metallic glasses are closely related to the manipulation of the operation of shear deformation units (i.e. ‘shear transformation zones (STZs)’ [2]) besides the control of mature shear bands. Overall, the modulation of multi-scale ‘shear avalanches’ in metallic glasses, ranging from nm-scale shear transformations to macroscopic shear banding, is a key issue for improving the ductility of such alloys.

Here we suggest a novel route for modulating shear avalanches and plasticity of metallic glasses in alloy systems with a metastable miscibility gap. From miscibility gaps in multicomponent systems, phase separating metallic glasses (PS-MGs) have been reported in various alloy systems such as La-Zr-Cu-Ni-Al [25], Cu-(Zr,Hf)-(Y,Gd)-Al [18,19], (Ti,Zr)-Y-Al-Co [26], Gd-Ti-Al-(Co,Cu) [27], Gd-(Hf,Ti,Y)-Co-Al [28,29], Ni-Nb-Y [30] and Gd-Zr-Al-Ni [31]. Although, the metallic glasses with dual amorphous phases were introduced as a novel amorphous-amorphous composite structure with enhanced mechanical properties in very limited cases [32], phase separation in glass-forming system, in general, causes to deteriorate both ductility and strength as compared to monolithic metallic glasses, which attributed to weak phase interfaces between the adjacent amorphous phases. However, the Cu-Zr-Al-Y PS-MG-forming system particularly exhibit a fine scale phase separation ranging over a few tens of nanometers and pronounced bending ductility being folded 180° without fracture for ribbon-type sample. Here, we systematically investigate the microstructure and deformation behavior of the Cu-Zr-Al-Y metallic glasses especially focusing on alloys with low Y contents (≤ 15 at.%). The presence of chemically heterogeneous substructures in the fully amorphous state depending on alloy compositions were confirmed by various structural analyses, and their role on the deformation behavior was examined via multi-scale mechanical tests including nanoindentation tests, micropillar compression tests and macro-scale bending tests. Based on the results, we propose a novel strategy for enhancing the plasticity of metallic glass-forming alloys via formation of spinodal-like nanoscale networks of chemical heterogeneities without pronounced sharp interfaces.

2. Experimental

2.1. Sample preparation

$\text{Cu}_{46}\text{Zr}_{47-x}\text{Al}_7\text{Y}_x$ ($x = 0, 2, 5, 10, 15, 20, 25, 30, 35, 47$ at.%) alloy ingots were prepared by arc-melting with high-purity elements of Cu (99.9%), Zr (99.9%), Al (99.9%), and Y (99.9%) under Ti-gettered argon atmosphere. Rapidly solidified ribbons were prepared by melt-spinning technique. The alloy ingots were re-melted in a quartz tube in an induction heater, and were ejected with an overpressure of 50 kPa through a 0.5 mm-diameter circular nozzle onto a copper wheel rotating with a surface velocity of 40 m/s. The dimension of the as-spun ribbons was 2 ± 0.2 mm in width and 40 ± 5 μm in thickness.

2.2. Microstructural characterization

The amorphous structure for the as-spun ribbon samples was

confirmed by X-ray diffraction (XRD; Bruker D2 Phaser) using monochromatic Cu K α radiation. The thermal behavior of the as-cast ribbons was investigated by differential scanning calorimetry (DSC; Perkin Elmer DSC 7) at a heating rate of 40 K/min. Scanning electron microscopy (SEM) observation was performed at a low acceleration voltage of 2 kV using a field-emission SEM (Zeiss CrossBeam 1540EsB) equipped with an in-lens detector.

SANS experiments were conducted using a 40 m SANS instrument [33] at the High-Flux Advanced Neutron Application Reactor (HANARO) at the Korea Atomic Energy Research Institute (KAERI). A monochromated cold neutron beam with an average wavelength 6 Å was irradiated to the ribbon sample packed tightly inside ϕ 8 mm \times t 1.5 mm volume in a cadmium holder. Three different sample-to-detector distances (SDD = 17.3, 6.7 and 1.15 m) setups were applied for measurement in wide q -range. After necessary data reduction processes for open beam scattering, transmission and detector inhomogeneities, the corrected scattering intensity functions were normalized to the absolute intensity scale.

Needle-shaped specimens for atom probe tomography (APT), having radii of curvature smaller than 100 nm, were prepared using a dual-beam FIB system (FEI Helios Nano-Lab 600i). A wedge-shaped piece of the sample was taken from the center area of the ribbon cross-section in a standard FIB lift-out procedure [34], placed on a Si micro-tip array, and subjected to annular FIB milling procedure at a low acceleration voltage of 30 kV (0.23 nA). Final polishing was done at 5 kV (40 pA) to minimize Ga + implantation into the samples and maintain it at a negligible level. APT analyses were carried out using a LEAP 3000 \times HR system (Cameca Instruments) in laser-pulsed mode at 100 kHz pulse repetition rate, 0.5% target evaporation, 0.4 nJ energy and 70 K. The APT data were reconstructed and evaluated using IVAS software provided by Cameca Instruments. Compositional frequency distributions are obtained by a grid-based counting algorithm [35,36] using a bin size of 300 atoms.

2.3. Mechanical testing

Nanoindentation tests were carried out on the finely polished cross-sections of ribbon samples using a nanomechanical tester (Hysitron TI 750 TriboIndenter) in a load-controlled test condition. In order to obtain an average hardness value of each ribbon sample, nanoindentation tests were repeated for 20 times per samples using Berkovich diamond tip. Standard deviations were used as error ranges. In order to analyze shear avalanches statistically in the selected ribbon samples, repeated nanoindentation tests were conducted for 150 times per sample using a conical-type diamond tip with a 2 μm radius. For a single indent, the indentation force was (i) increased up to peak force of 5 mN in 5 s at constant loading rate, (ii) remained at the peak force for 2 s, and (iii) was finally unloaded in 5 s. The deviations were used as error ranges. The strain burst sizes of pop-ins were collected from the resulting load-displacement curves using a MATLAB-based code.

Micropillar samples were fabricated by FIB (FEI Nova 600 Nanolab) at the center region of ribbon cross-sections. Annular FIB milling procedure was conducted using an acceleration voltage of 30 kV and with ion beam current controlled from 5 nA to 100 pA to minimize the taper angle of the pillars to a value below 1.5°. The final dimension of the cylindrical pillars was ϕ 1.8 ± 0.05 μm \times H 3.9 ± 0.1 μm (aspect ratio ~ 2.167). The fabricated pillars were compressed in a load-controlled mode with a constant loading rate of 10 $\mu\text{N/s}$ using *in situ* mechanical tester (Hysitron Picoindenter PI-85) inside a field-emission SEM (FEI Quanta 250). A flat-punch type diamond tip with flat surface diameter = 10 μm was used for the compression tests. Before compression, the diamond tip contacted with the pillars forcing small preload of 2 μN and an average drift

rate was measured for 20 s, for drift correction.

Bending deformation tests of ribbon samples were conducted by a custom-made apparatus consisting of a pair of parallel platens; one fixed and the other one movable. The position of the movable platen (the distance between the platens) and its driving speed (v) were precisely controlled in a resolution $< 1 \mu\text{m}$ by an electric motor and a LabVIEW-based software. Edges of ribbon samples were finely polished before bending. Each end of the ribbon sample was fixed to each platen respectively, and was bent between the platens by approaching the movable platen to the fixed platen. The ribbons tested in this study were bent until reaching an equivalent strain ($\epsilon = 0.05$) and strain rate ($\dot{\epsilon} = 0.005$) condition by varying the end position and driving speed of the movable platen depending on sample thickness. The bent ribbons were removed from the platens after test and the kink angles of the ribbons were measured by optical microscope observation at bent point.

3. Results

3.1. Microstructural characterization of Cu-Zr-Al-Y as-spun ribbons

3.1.1. DSC analysis

Fig. 1 shows the DSC thermograms of $\text{Cu}_{46}\text{Zr}_{47-x}\text{Al}_7\text{Y}_x$ ($0 \leq x \leq 47$ at.%) as-spun alloy ribbons. In this paper, an alloy sample with $x = \lambda$ at.% will be denoted as ‘Y λ ’ (e.g. Y15 for $\text{Cu}_{46}\text{Zr}_{35}\text{Al}_7\text{Y}_{15}$). For alloys with $x = 15$ –35 at.%, the formation of two different amorphous phases by phase separation can be confirmed by separate crystallization behaviors observed in the DSC measurements. Each exothermic peak corresponding to the crystallization of a Y-rich amorphous phase and a Zr-rich amorphous phase appears at the temperatures close to the crystallization peaks of the alloys Y47 and Y0, respectively. Alloys with $x = 0$ –10 at.% have a

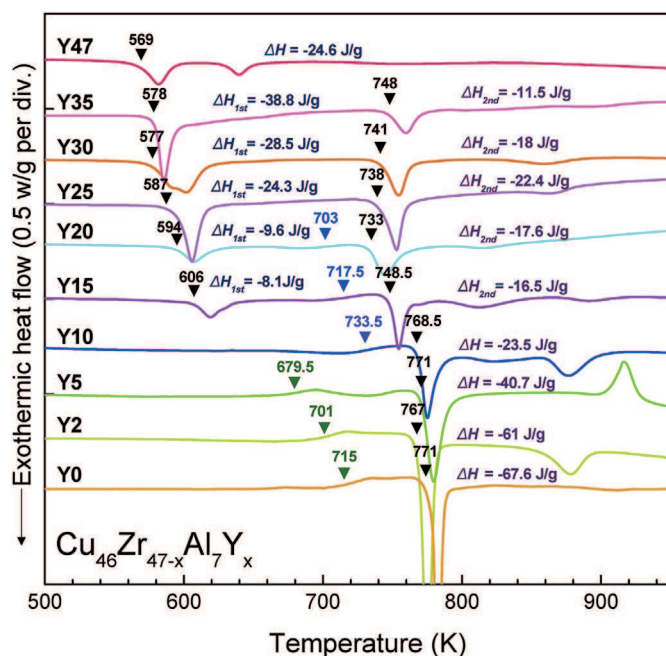


Fig. 1. DSC traces obtained from as-spun $\text{Cu}_{46}\text{Zr}_{47-x}\text{Al}_7\text{Y}_x$ ($x = 0, 2, 5, 10, 15, 20, 25, 30, 35, 47$ at.%) alloy ribbons. The numbers with arrows are the characteristic temperatures of the corresponding alloy ribbons; (colored) glass transition temperatures, (black) crystallization onset temperatures. ΔH values are the reaction enthalpies associated with exothermic crystallization peaks. The DSC results of the alloys with $x = 0, 2, 5, 10, 15, 25$ and 35 at.% were reused from Ref. [18] with permission. ©2006. Elsevier. (For interpretation of the references to colour in this figure legend, the reader is referred to the web version of this article.)

single exothermic peak in the range of 767–771 K with a clear glass transition temperature (T_g), respectively, which typically corresponds to the crystallization of a monolithic Zr-rich amorphous phase.

3.1.2. SEM observation

The microstructures of Cu-based metallic glasses are difficult to observe without artifacts via electron microscopy, due to rapid surface oxidation in the atmosphere after polishing [37]. Moreover, the nanoscale phase separation between the Zr-rich and Y-rich amorphous phases cannot be readily distinguished in terms of Z-contrast images obtained by a normal backscattered electron detector in SEM, because of the small difference in atomic weight between Zr and Y with their neighboring atomic numbers and a lack of resolution. In this study, *in situ* ion beam polishing and imaging techniques in a FIB/SEM dual beam system were applied for observing the microstructure of the as-spun Cu-Zr-Al-Y alloy ribbons. In order to avoid surface oxidation and artifacts, the cross-section of a ribbon was polished at the edge by Ga^+ ion beam with stepwise ion beam currents from 5 nA to 300 pA. Then, a weak ion beam of 50 pA perpendicular to the observation plane was applied for a short time below 3 s, which enhances the contrast of separated amorphous phases via an ion-beam etching effect. The etched cross-section was observed using an in-lens type detector in SEM directly without exposure to air. The in-lens detector collects type-I secondary electrons (SE1) emitted from the sample surface with a high emission angle and observes a sample at a short working distance (2–5 mm) and a low acceleration voltage of 2 kV [38]. This enables to obtain images with the amplified contrast sensitive to both the phase difference and surface roughness, as well as with high resolution [39].

The resulting images of the $\text{Cu}_{46}\text{Zr}_{47-x}\text{Al}_7\text{Y}_x$ alloy ribbons are shown in Fig. 2. Before applying the ion-beam etching process all ribbon samples show only extremely weak contrast, making it hard to distinguish the different amorphous phases, while the samples with $15 \leq x \leq 35$ at.% reveal clear contrast between the phases after etching. The effect of etching may be attributed to the difference in etching rate by the ion beam between the two phases. The images in Fig. 2 were obtained at the center area of the cross section between the wheel side and the free side of the ribbons. The darker phase with a larger fraction in the alloys with relatively high Zr composition corresponds to the Zr-rich amorphous phase and the opposite one to the Y-rich amorphous phase. Fig. 2(b–f) show a clear size variation of the separated phases such that the average phase width is the largest in the alloy Y25 and decreases with shifting the alloy composition from $x = 25$ at.%. Fig. 2(b) for the alloy Y15 shows fine Y-rich secondary phases with a phase width below 25 nm in the Zr-rich matrix. The alloy Y10 does not exhibit phase contrast in SEM resolution, as shown in Fig. 2(a).

3.1.3. SANS analysis

In contrast to microscopic observation representing a local area at micrometer scale, small-angle scattering (SAS) measurements can investigate the size of chemical heterogeneities within a large volume over millimeter scale. A scattering pattern in an SAS measurement originates from the difference of the scattering length density among the phases in a sample, where the scattering length density of a phase is determined by its chemical composition, density and the scattering lengths of the constituent elements. The neutron scattering lengths for the atoms are independent of their atomic numbers, while the X-ray scattering lengths are approximately proportional to the atomic numbers. As incident beam for using SAS, therefore, the neutron beam has an advantage for distinguishing Y-rich amorphous phase from Zr-rich amorphous phase in the Cu-Zr-Al-Y alloys as compared to X-ray beam. Fig. 3(a) shows

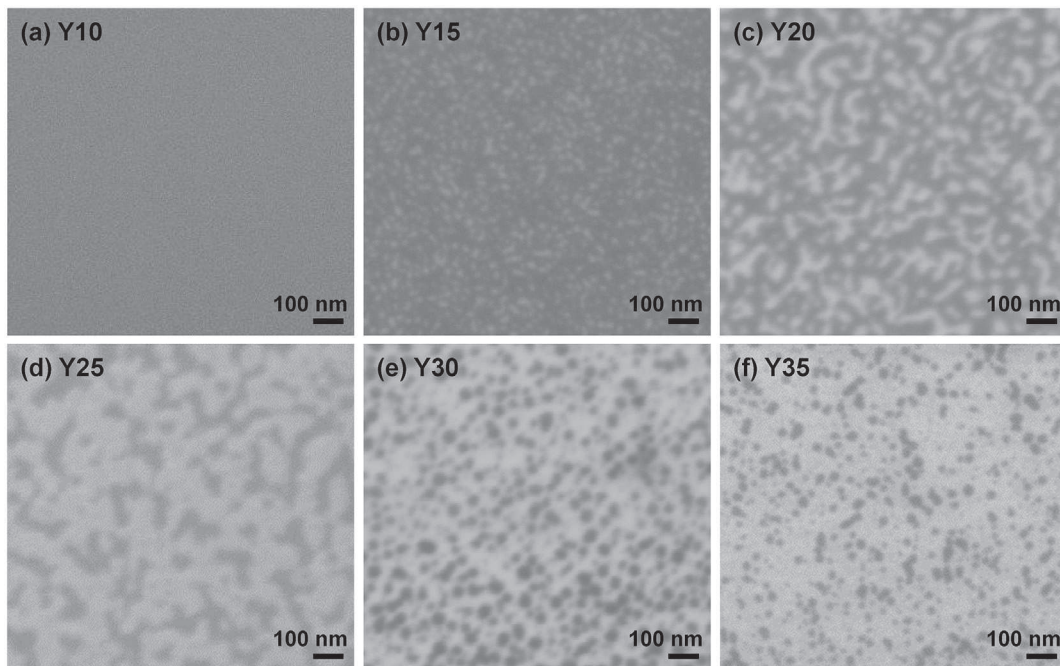


Fig. 2. SE images of $\text{Cu}_{46}\text{Zr}_{47-x}\text{Al}_7\text{Y}_x$ ($x = 10, 15, 20, 25, 30, 35$ at.%) alloy ribbons after weak-ion beam etching treatment, obtained by in-lens SE detector. The scale bars are for 100 nm. The phase with darker contrast is Zr-rich amorphous phases, while the opposite is Y-rich amorphous phases.

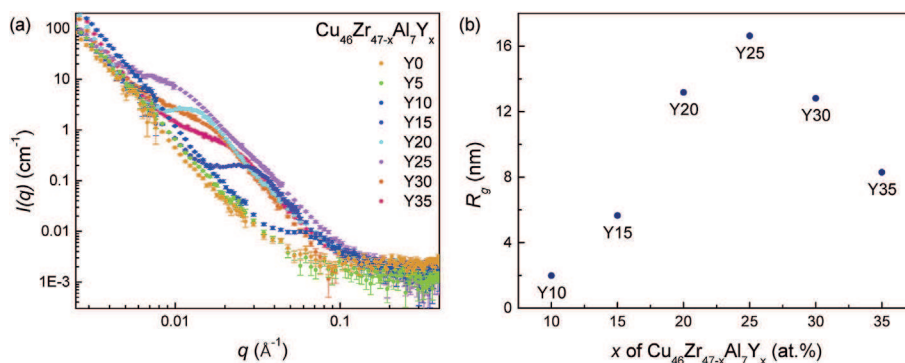


Fig. 3. (a) SANS patterns of as-spun $\text{Cu}_{46}\text{Zr}_{47-x}\text{Al}_7\text{Y}_x$ ($x = 0, 5, 10, 15, 20, 25, 30, 35$ at.%) alloy ribbons. (b) Radii of gyration (R_g) for chemical heterogeneities in the alloy ribbons, estimated from the fitting of the SANS patterns using Guinier approximation.

small-angle neutron scattering (SANS) patterns of the $\text{Cu}_{46}\text{Zr}_{47-x}\text{Al}_7\text{Y}_x$ as-spun alloy ribbons. The scattering patterns of the alloys Y0 and Y5 exhibit only a power-law region at low q -range, which are the typical patterns from monolithic metallic glasses without any chemical heterogeneities over the minimum detectable size in SANS (~ 1 nm). On the other hand, the scattering patterns of the ribbon samples with $10 \leq x \leq 35$ at.% have clear shoulders from their chemically inhomogeneous structures. Interestingly, the alloy Y10 reveals a shoulder at a relatively large q -range, which means the existence of chemical heterogeneities in a few-nanometer scale not detected in the DSC analysis or SEM observation. The individual scattering patterns are fitted using a unified Guinier/power-law model [40,41] to estimate the average size of separated phases. The radii of gyration (R_g) obtained from a Guinier law derived model [40,42] are displayed depending on Y composition in Fig. 3(b). The variation of R_g values which are proportional to the average phase width [42] in the alloys corresponds well with the SEM images of Fig. 2.

3.1.4. APT analysis

Placing the focus on the microstructural evolution in the alloys with relatively small Y compositions, atom probe tomography (APT) analyses were performed for the alloy ribbons Y0, Y5, Y10 and Y15. The APT reconstructions of the four samples are shown in Fig. 4. Cu, Zr, Al and Y are presented in yellow, blue, purple and red colors, respectively. The bottom row images in Fig. 4 are 2 nm-thick slices for the alloys Y0, Y5 and Y10 and a 5 nm-thick slice for the alloy Y15. The APT maps of the alloys Y0 and Y5 do not exhibit any obvious clustering of elements as shown in Fig. 4(a, b), while the APT maps of the alloys Y10 and Y15 shown in Fig. 4(c, d) reveal Y-enriched regions (position of Y atoms shown by red dots). The APT map of the alloy Y10 exhibits relatively diffuse interfaces between Y-rich regions and the matrix, where the approximate average width of Y-rich regions is ~ 5 nm. The morphology of Y-rich regions in the alloy Y10 is difficult to be defined due to their diffuse interfaces but they form bi-continuous networks by continuous compositional fluctuation, rather than isolated morphology. In

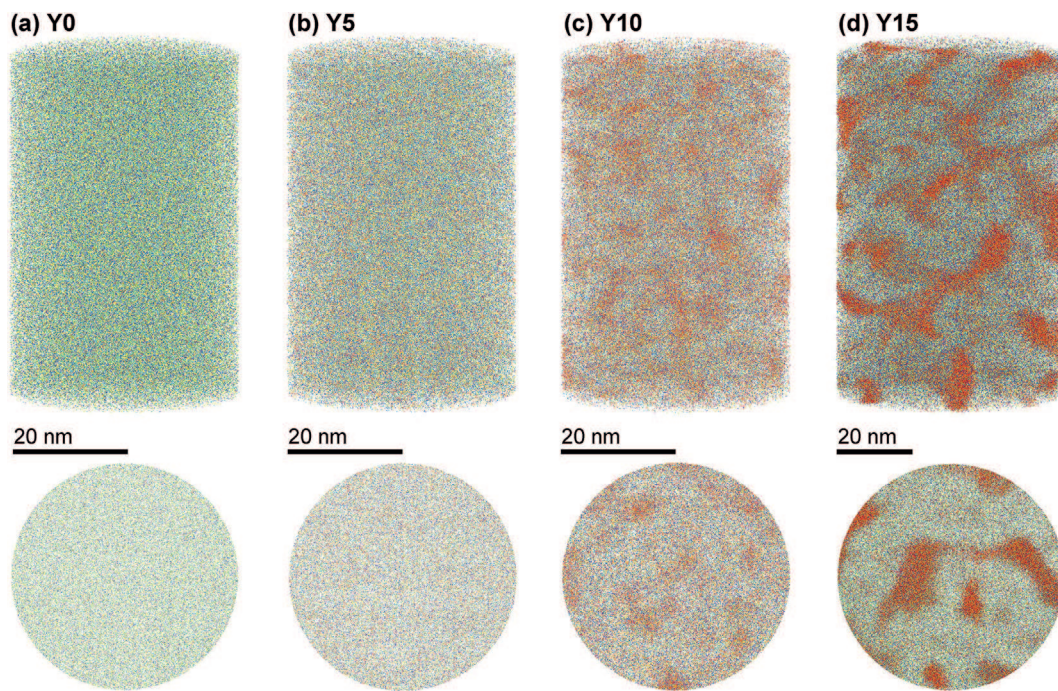


Fig. 4. APT reconstructions showing the distribution of the alloy metallic elements (Cu-yellow; Zr-blue; Al-purple; Y-red) in the as-spun alloy ribbons of (a) Y0, (b) Y5, (c) Y10 and (d) Y15. The upper images are three-dimensional views for cylindrical regions, and the lower images are 2 nm-thick virtual slices of the respective reconstructions. (For interpretation of the references to colour in this figure legend, the reader is referred to the web version of this article.)

contrast, the APT map of the alloy Y15 shows more pronounced Y-enrichments with an average width of ~ 10 nm and clear interfaces between Y-enrichments and the matrix (Refer to videos in Supplementary Materials for clear visions of three-dimensional microstructures).

Supplementary video related to this article can be found at <http://dx.doi.org/10.1016/j.actamat.2017.08.002>.

Comparative analyses between the frequency distributions of elemental concentrations in APT data and binomial distributions are useful for quantifying fine scale clustering effects of constituent elements in alloys [36]. Fig. 5 represents the results of the frequency distribution analysis for the APT data sets retrieved for the alloys Y0, Y5, Y10 and Y15, respectively. The deviation of the experimental frequency distribution curves (Solid curves in Fig. 5) from binomial distribution functions (Dashed curves in Fig. 5) gives the p and μ -value, with which the chemical homogeneity of the samples can be assessed. A p -value of 0.05 is commonly used standard value to reject the null hypothesis in statistical hypothesis testing. Thus, if the p -value is less than 0.05, it is assumed that the alloy is not homogeneous and that elemental clustering within the alloy may prevail [36]. μ varies between 0 and 1, where 0 indicates a random homogeneous distribution and 1 indicates a complete ordering of the constituent atoms [36]. The p -values far above 0.05 and small μ values near zero for the alloy Y0 indicate uniform elemental distribution as characteristic for a monolithic metallic glass. The binomial distribution function and the experimental frequency distribution of the alloy Y0 show only very little deviation from each other as shown in Fig. 5(a). With the small addition of Y to the Y0 composition, the p -values for Zr and Y distribution in the alloy Y5 drop to near or less than 0.05, while the μ values for all constituent elements are slightly increased. The experimental distribution shows only very little deviation from a binomial distribution function, as shown in Fig. 5(b). These observations indicate that a monolithic amorphous phase without any nanoscale heterogeneities or correlations is formed, but that chemical

heterogeneities exist at the atomic scale in the alloy Y5 [18]. With the further addition of Y, the extremely small p -values and the drastic increase of the μ values for the atomic distributions in the alloy Y10 reveal the presence of significant clustering although the frequency distribution curves do not show clear peak separation (Fig. 5(c)). Especially, the large μ values near 1 for Zr and Y distributions in the alloy Y10 indicate the intense compositional fluctuation due to their positive heat of mixing relation. For the alloy Y15 shown in Fig. 5(d), the frequency distribution curves of all constituent elements exhibit peak separation into two peaks. The small p -values and μ values close to 1 also reflect the clear phase-separated structure of the alloy Y15. From the concentrations of the peak maxima, the compositions of the Zr-rich and the Y-rich amorphous phases in the alloy Y15 are estimated to be $\text{Cu}_{42.3}\text{Zr}_{44.3}\text{Al}_{8.8}\text{Y}_{4.6}$ and $\text{Cu}_{55.7}\text{Zr}_{15.1}\text{Al}_{3.6}\text{Y}_{25.6}$ in atomic percent, respectively.

The proxigram is a profile of local atomic concentrations versus proximity to an interface, and is an accurate method for illustrating concentration variations in the direction passing through an interface [43]. The proxigrams with respect to interfaces between Zr-rich and Y-rich regions in the alloys Y10 and Y15 are shown in Fig. 6. Strictly speaking, the two regions in the alloy Y10 have no clear interface, but the interface for the proxigram analysis is set empirically to be the position with Y = 9 at.%, where the proxigram result shows clear variations of concentrations. The interface in the alloy Y15 is set to the position with Y = 13 at.% between the two peaks in the frequency distribution of Y in Fig. 5(d). The concentration profiles in the proxigram of the alloy Y10 (Fig. 6(a)) reveal that the concentrations of the four elements change consistently and a range with a constant composition exists in neither the Zr-rich nor the Y-rich regions. In contrast, the concentration profiles in the proxigram of the alloy Y15 (Fig. 6(b)) show relatively drastic compositional change at the region near the interface and chemically homogeneous regions (or “phases”) with specific compositions exist inside both Zr-rich and Y-rich regions.

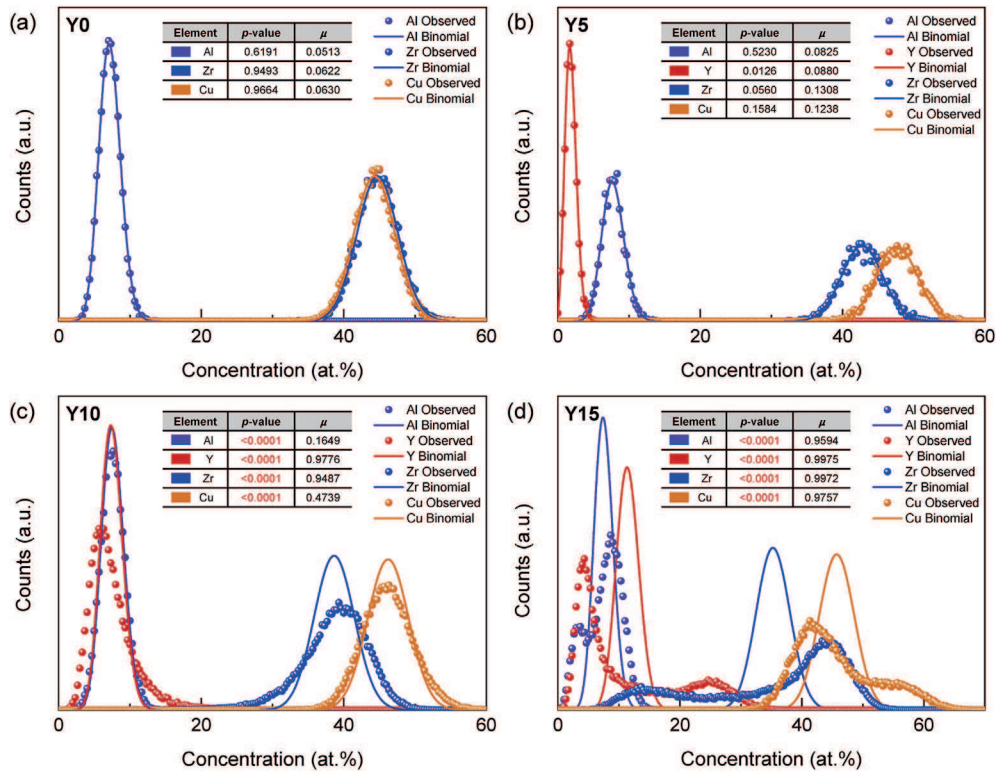


Fig. 5. Statistical binomial frequency distribution analysis results for the APT tips of (a) Y0, (b) Y5, (c) Y10 and (d) Y15. A bin size for frequency distributions is 0.33 at.%. The quality of the binomial fit was quantified using p -value and μ parameters, as listed in the inset tables.

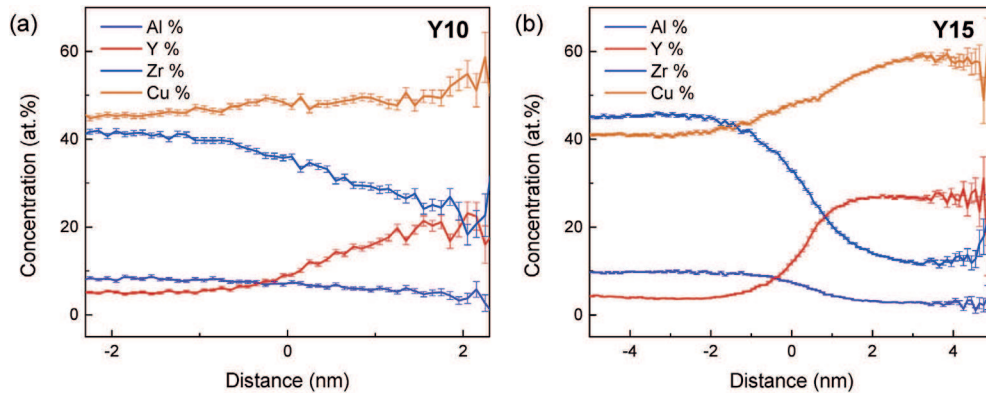


Fig. 6. Proxigrams with respect to interfaces between Zr-rich region and Y-rich region in the alloys (a) Y10 and (b) Y15, calculated with a bin size of 0.3 nm. The interface (distance = 0) for the proxigram analysis is set to be the position with Y = 9 at.% (a) and 13 at.% (b), respectively, from the frequency distribution of Y.

3.2. Deformation behavior of Cu-Zr-Al-Y as-spun ribbons

The variation in local compositional features in the Cu-Zr-Al-Y metallic glasses, i.e. of the chemical heterogeneity depending on Y compositions was expected to significantly affect the deformation behavior of the alloys. In this study, the deformation behavior of the Cu-Zr-Al-Y alloys is investigated by multi-scale testing including i) hardness measurement, ii) shear avalanche analysis via nanoindentation tests (nanoscale), iii) micropillar compression tests (microscale) and iv) bending tests of ribbons (macroscale).

3.2.1. Nanoindentation tests and statistical analysis of shear avalanches

Fig. 7 shows the hardness values of as-spun ribbons measured by nanoindentation. The effective mechanical properties of an ideal

phase mixture can be estimated by using a rule of mixtures [44,45] in terms of its constituent component phases. The upper and lower bounds (\bar{H}_{up} , \bar{H}_{low}) for the effective hardness \bar{H} of a mixture can be approximated either by a rule of mixtures based on iso-strain assumption [44] ($\bar{H}_{up} = f_A H_A + f_B H_B$) or iso-stress approach [45] ($\bar{H}_{low} = (f_A/H_A + f_B/H_B)^{-1}$) [46]. H and f are the hardness and fraction of each component phase, respectively, and the subscripts denote the component phases. Assuming the $\text{Cu}_{46}\text{Zr}_{47-x}\text{Al}_7\text{Y}_x$ alloys as mixtures of the alloy Y0 (\approx Zr-rich amorphous phase) and the alloy Y47 (\approx Y-rich amorphous phase), the variation of \bar{H} with Y content (x) in the $\text{Cu}_{46}\text{Zr}_{47-x}\text{Al}_7\text{Y}_x$ alloys is visualized as gray dashed lines in Fig. 7. The measured hardness values of the alloys (purple data points) exhibit deviations from the estimated \bar{H} depending on x . The hardness of alloy Y5 is close to the lower bound of \bar{H} and that of alloy Y10 has a relatively small deviation from \bar{H} compared to the

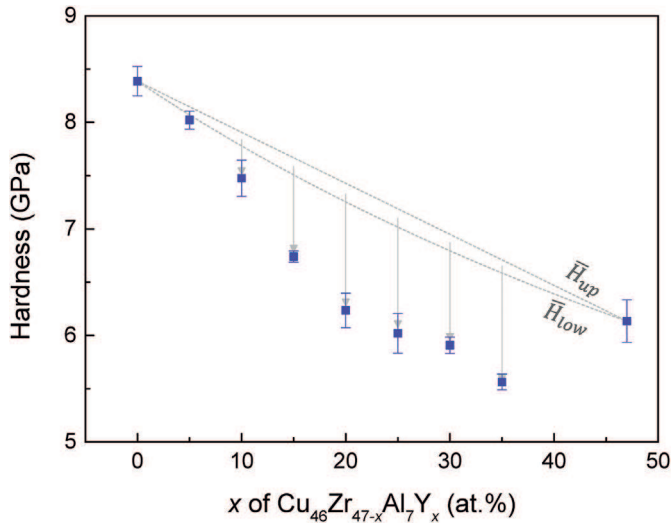


Fig. 7. Hardness of $\text{Cu}_{46}\text{Zr}_{47-x}\text{Al}_7\text{Y}_x$ alloy ribbons, obtained from nanoindentation tests. The values are average values from 20 repeated tests, and standard deviations were used as error ranges.

alloys with higher Y contents. The alloys with $15 \leq x \leq 35$ at.% have far lower hardness values (~ 1 GPa lower) than \bar{H} estimated by the rule of mixtures.

We investigated the changes in intermittent shear avalanches during plastic deformation in the alloys Y0, Y5, Y10 and Y15 by mapping pop-in events in the nanoindentation results. Each pop-in event reflects the activation of STZs [47] or the process of shear band formation and propagation [48], and the displacement burst size in a pop-in event reflects the size of that shear deformation. In order to statistically analyze the shear avalanches in the alloys, at least 150 pop-ins per alloy were collected from the load (F) - displacement (h) curves obtained by nanoindentation. The collection process of pop-in events is described in Refs. [49,50]. The size of the displacement burst (Δh) associated with a pop-in event was normalized as strain burst size, $S = \Delta h/h$, to eliminate statistical errors [48,50]. The distributions of strain burst size for each sample are presented as histograms in Fig. 8. The monolithic amorphous alloy Y0 exhibits a strain burst size distribution in a relatively broad S range, with a trend of decreasing number fraction with increasing S . For the alloy Y5, the fraction of small-sized strain burst (< 0.02) is slightly increased as compared to the alloy Y0. The alloys Y10 and Y15 have a drastically increased fraction of small-sized strain bursts, concentrated at S ranges below ~ 0.01 . The statistical analysis for the distributions of strain burst sizes is discussed further in section 4.2.

3.2.2. Compression tests of micropillars

In order to investigate the effect of amorphous chemical heterogeneity on the deformation behavior of the alloys at the microscale, we performed micropillar compression tests on the alloys Y0, Y5, Y10 and Y15. The micropillars were fabricated by FIB-milling in the dimensions described in the inset of Fig. 9. The pillars were uniaxially compressed by an *in situ* mechanical tester inside a SEM in load-controlled mode, which enables to clearly observe pop-in strain bursts generated by shear banding. Fig. 9 shows representative stress-strain curves of Y0, Y5, Y10 and Y15 micropillars. Due to the tapered shape of the pillars, engineering stresses in Fig. 9 were estimated using the diameter measured close to the top surface [51] ($= 1.85 \mu\text{m}$ at 90% of the height of the pillar). For the Y0 and Y5 pillars, series of pop-ins with sharp strain bursts are observed in the stress-strain curves. These pop-in events originate

from rapid localized deformation along mature shear bands, which generally occur in monolithic metallic glasses [52,53]. The pop-ins in the stress-strain curves of the alloys Y10 and Y15, however, include a large number of data points, which indicates much more sluggish shear band deformation in the alloys Y10 and Y15. Especially the alloys Y10 and Y15 show wavy stress-strain behavior in contrast to the sharp pop-in behavior found for the alloys Y0 and Y5. The morphologies of the compressed pillars also reveal clear differences in deformation behavior among the specimens as shown in Fig. 10. The compressed Y0 pillar has only a few shear bands developed in similar directions (Fig. 10(a)). A slightly increased number of shear bands appears in the Y5 pillar, but they also have similar slip directions (Fig. 10(b)). On the other hand, in the case of the Y10 and Y15 pillars, multiple shear bands form shear steps in various directions (Fig. 10(c,d)), which may cause sluggish deformation behavior in the samples as observed in Fig. 9.

3.2.3. Flow stress analysis via bending tests of alloy ribbons

The deformation behavior of the alloys at the macroscale has been investigated by kink angle measurements after bending of the ribbons. Fig. 11(a) describes the bending test procedure: A ribbon-shaped sample was fixed between two platens (one fixed and the other movable) and bent by approaching the movable platen to the fixed platen. The distance between the platens and the approaching velocity of the movable platen were precisely controlled by an electric motor. For a ribbon of thickness d between platens with separation D , the strain ε and strain rate $\dot{\varepsilon}$ at the curved surface of the ribbon is approximately given by Ref. [54].

$$\varepsilon = \frac{d}{D-d} \quad (1)$$

$$\dot{\varepsilon} = \left| \frac{d\varepsilon}{dt} \right| = \frac{vd}{(D-d)^2} \quad (2)$$

where v is the approaching velocity of the movable platen, which is constant during a test. The ribbons were bent until reaching simultaneously the $\varepsilon = 0.05$ and $\dot{\varepsilon} = 0.005$ conditions by varying the minimum D (the end position of the movable platen) and v depending on sample thickness.

The kink angle (springback angle, α in Fig. 11(b)) of the bent ribbons was measured after removing the ribbons from the platens. For the materials with the absence of work hardening or softening, the kink angle α (in radians) has a relation with the flow stress σ_f of plastic deformation as follows [55].

$$\frac{1 - \alpha/\pi}{Dr} = -\frac{1}{2} \left(\frac{\sigma_f}{Ed} \right)^3 Dr^2 + \frac{3}{2} \left(\frac{\sigma_f}{Ed} \right) \quad (3)$$

E is Young's modulus and $D' = D - d$. Young's moduli of the Cu-Zr-Al-Y alloy ribbons were measured by nanoindentation [56]. In order to compute the Young's modulus of a sample from the reduced modulus obtained by nanoindentation tests, the modulus and Poisson's ratio of a diamond indenter tip of 1141 GPa and 0.07 [57], respectively, were used. The Poisson's ratios of the alloy ribbons were assumed to be 0.375 ± 0.005 [58,59], which have only a minor influence within $\pm 0.5\%$ on σ_f . Flow stresses of bending plastic deformation at curved surface are estimated from kink angle measurement depending on alloy composition of the Cu-Zr-Al-Y ribbons, as shown in Fig. 11(c). The flow stress of the alloys clearly decreases with increasing Y content for $x \leq 10$ at.%, while it remains at a constant level in those alloys with $x \geq 15$ at.%. These results reveal that the deformation behavior of the Cu-Zr-Al-Y ribbons are significantly affected by the presence of internal phase interfaces as well as by the presence of the associated

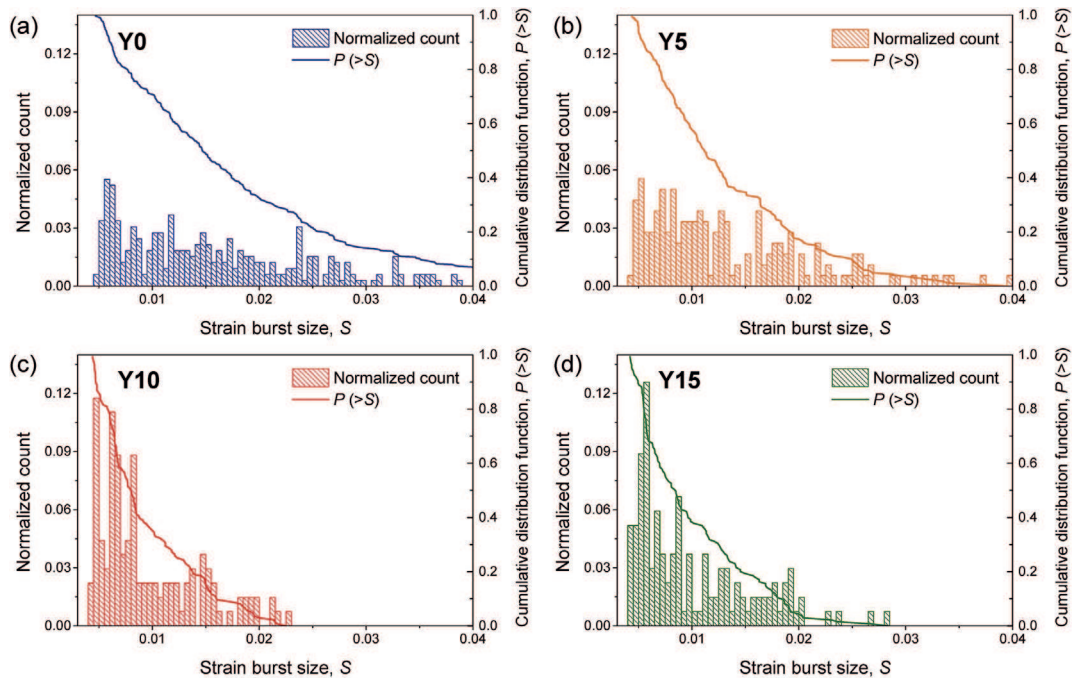


Fig. 8. Histograms and cumulative distribution curves of strain burst sizes (S) collected from the series of nanoindentation tests with the alloys (a) Y0, (b) Y5, (c) Y10 and (d) Y15. The bin size for S in histograms is 5×10^{-4} .

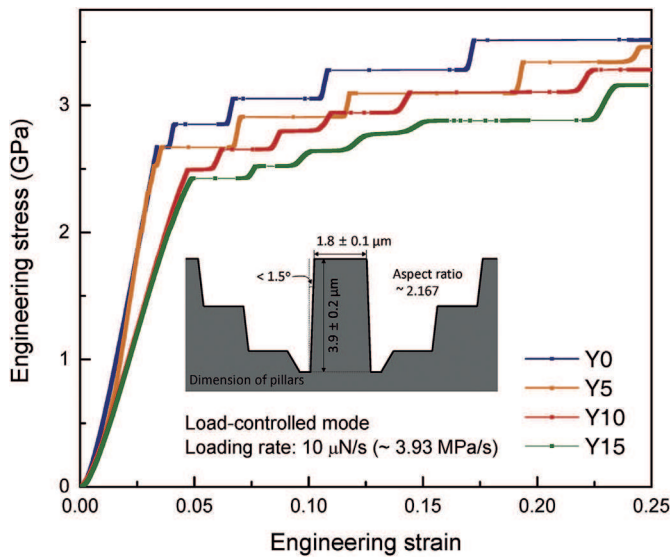


Fig. 9. Engineering stress–strain curves for compressed $\text{Cu}_{46}\text{Zr}_{47-x}\text{Al}_7\text{Y}_x$ ($x = 0, 5, 10, 15$ at.%) micropillars. The inset schematic diagram represents the dimension of the micropillars before compression.

chemical heterogeneity, as will be discussed further in section 4.2.

4. Discussion

4.1. Thermodynamic calculation of the metastable miscibility gap and its correlation with the microstructures of Cu–Zr–Al–Y as-spun ribbons

The microstructural analysis results in Figs. 1–6 clearly reveal the presence of compositionally heterogeneous microstructures in Cu–Zr–Al–Y metallic glasses. The size scale of these features depends

on alloy composition. Especially in those alloys where $Y \leq 15$ at.%, compositional heterogeneities occur at an extremely fine size scale below ~ 15 nm. The alloy Y0, i.e. the material without any yttrium, exhibits a typical monolithic amorphous structure with chemically homogeneous and random atomic distribution, as also shown by the single crystallization peak in the DSC result (Fig. 1), the SANS pattern without appearance of a Guinier region from nanoscale scatterers (Fig. 3(a)), and the p -values far above 0.05 and small μ values near zero in the frequency distribution analysis result (Fig. 5(a)). With a small substitution of Zr by Y (5 at.%) in the Y0 alloy, the alloy Y5 also forms a monolithic metallic glass without any detectable compositional heterogeneity at a scale above 1 nm, which is the minimum detection limit of SANS. However, the p -values near and below 0.05 for Zr and Y (Fig. 5(b)), respectively, suggest the presence of local chemical fluctuation at the nearly atomic scale [18], i.e. local clustering of Zr and Y [36] in the Y5 alloy. With the further addition of Y up to 10 at.%, the chemical fluctuation intensifies to the scale of a few nanometers, as observed in the SANS pattern (Fig. 3) and the APT reconstruction image (Fig. 4(c)) of the alloy Y10. These nanoscale compositional fluctuations in the Y10 alloy are characterized by a continuous rather than abrupt variation in local composition (Fig. 6(a)). This means that the composition pattern does not show any sharp compositional changes over a narrow region such as observed for conventional phase interfaces. The next material in this row, the alloy Y15, is characterized by a clearly phase-separated microstructure where the compositionally homogeneous phases have sharp interfaces, as suggested by the clear peak separation in the frequency distribution analysis result (Fig. 5(d)) and by the steep compositional changes among the adjacent phases in the proxigram analysis (Fig. 6(b)). The average width of such chemical heterogeneity features can be approximated by $w = \sqrt{24/5}R_g$ when assuming that the structure consists of randomly connected cylindrical rods with a shape function $R_g^2 = w^2/8 + L^2/12$ [42] where L is the same length of all the rods and w is their cross-sectional diameter. When assuming that the heterogeneous microstructures observed in the

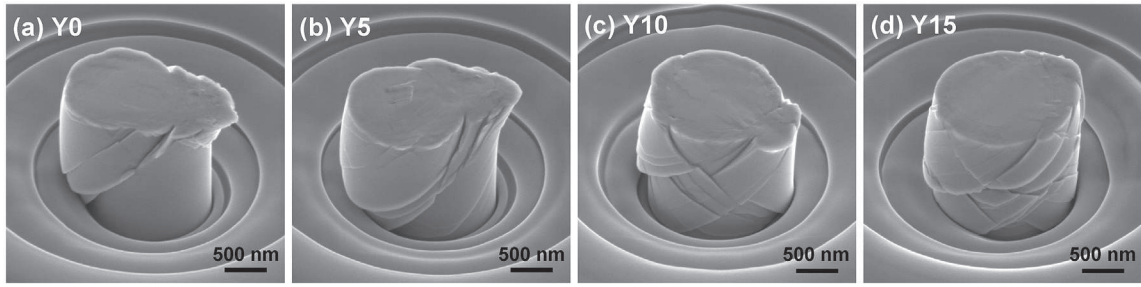


Fig. 10. SEM images of compressed micropillars, (a) Y0, (b) Y5, (c) Y10 and (d) Y15. The images were captured at a tilt angle of 45° to the longitudinal axis of the pillars. The scale bars are for 500 nm.

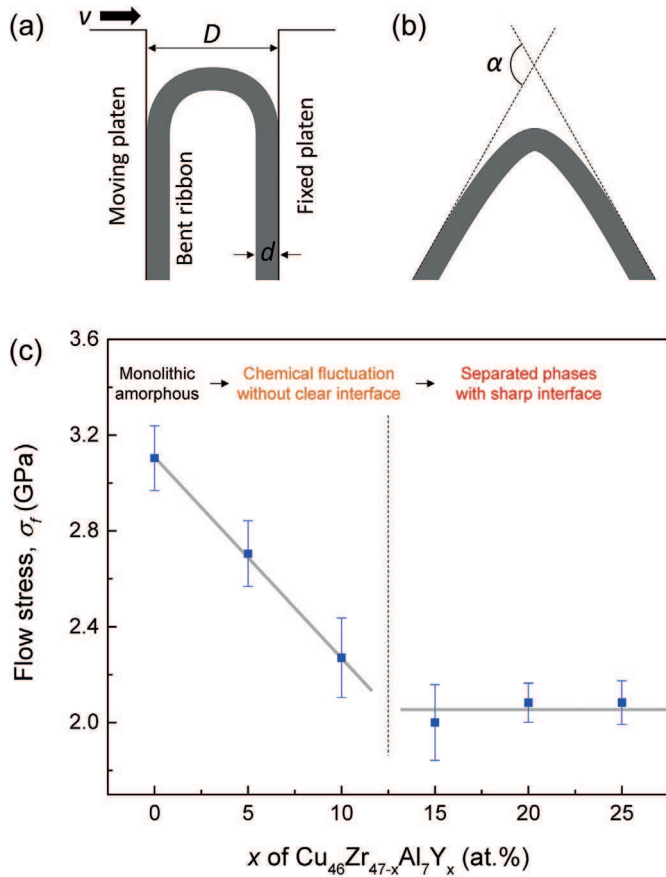


Fig. 11. Bending test results of Cu-Zr-Al-Y alloy ribbons. (a) Schematic illustration of ribbon bending test apparatus. (b) Definition of kink angle in an unloaded bent ribbon sample. (c) Flow stress (σ_f) in bending plastic deformation depending on Y composition of $\text{Cu}_{46}\text{Zr}_{47-x}\text{Al}_7\text{Y}_x$ alloy ribbons. The values are averaged through 10 measurements per alloy composition, and standard deviations were used as error ranges.

alloys Y10 and Y15 are spinodal-type interconnected structures, the average width of the heterogeneities is estimated to be 4.4 nm and 12.4 nm for the alloys Y10 and Y15, respectively, matching the results obtained by APT (Fig. 4(c,d)).

The miscibility gap and their dependence on alloy composition significantly affect the microstructural evolution and phase separation kinetics [27]. We thermodynamically assessed the metastable miscibility gap in the Cu-Zr-Al-Y quaternary alloy system using the CALPHAD method in conjunction with Thermo-Calc software. Phase separation occurs in a stable liquid state or in a metastable supercooled liquid state and the separate liquid phases form a PS-MG by solidifying into individual amorphous solids.

Hence, only the liquid-state interactions of the constituent elements have been considered in the thermodynamic calculations of the metastable miscibility gap in this system. The molar Gibbs free energy of a liquid solution phase can be expressed as a sum of i) the Gibbs free energy of the pure elements, ii) the Gibbs free energy changes contributed from the ideal mixing entropy and iii) the excess Gibbs free energy, as follows.

$$G^{Liq} = \sum_i x_i^0 G_i + RT \sum_i x_i \ln x_i + {}^{xs}G^{Liq} \quad (4)$$

where 0G_i is the molar Gibbs energy of the pure elements i ($=\text{Cu}, \text{Zr}, \text{Al}, \text{Y}$), and x_i is the mole fraction of element i . The excess Gibbs free energy, ${}^{xs}G$, is described by the quasi-regular solution model using the Redlich–Kister ansatz [60], i.e.,

$$\begin{aligned} {}^{xs}G^{Liq} = & x_{\text{Cu}}x_{\text{Y}} \sum_v L_{\text{Cu,Y}}^{Liq} (x_{\text{Cu}} - x_{\text{Y}})^v + x_{\text{Cu}}x_{\text{Zr}} \sum_v L_{\text{Cu,Zr}}^{Liq} (x_{\text{Cu}} - x_{\text{Zr}})^v \\ & + x_{\text{Al}}x_{\text{Cu}} \sum_v L_{\text{Al,Cu}}^{Liq} (x_{\text{Al}} - x_{\text{Cu}})^v \\ & + x_{\text{Al}}x_{\text{Zr}} \sum_v L_{\text{Al,Zr}}^{Liq} (x_{\text{Al}} - x_{\text{Zr}})^v + x_{\text{Al}}x_{\text{Y}} \sum_v L_{\text{Al,Y}}^{Liq} (x_{\text{Al}} - x_{\text{Y}})^v \\ & + x_{\text{Y}}x_{\text{Zr}} \sum_v L_{\text{Y,Zr}}^{Liq} (x_{\text{Y}} - x_{\text{Zr}})^v \end{aligned} \quad (5)$$

Where v is the order of the term considered and ${}^vL_{\text{A,B}}^{Liq}$ is the temperature and composition-dependent interaction parameter in liquid state for the A-B atomic pairs at the order v . The interaction parameters for the Cu-Y [61], Cu-Zr [62], Al-Cu [63], Al-Zr [64], Al-Y [65] and Y-Zr [66] binary pairs used in this study are listed in Table 1. The ternary and higher-order interactions in the Cu-Zr-Al-Y alloy system have not been considered here since they are unknown and may have only a minor effect on the result. The critical compositional border for spinodal decomposition is estimated based on the stability function [67], which expresses a spontaneous, i.e. spinodal decomposition between the inflection points, i.e.

$$\varphi = \begin{vmatrix} \frac{\partial^2 (G^{Liq}/RT)}{\partial X_{\text{Zr}}^2} & \frac{\partial^2 (G^{Liq}/RT)}{\partial X_{\text{Zr}} \partial X_{\text{Al}}} & \frac{\partial^2 (G^{Liq}/RT)}{\partial X_{\text{Zr}} \partial X_{\text{Y}}} \\ \frac{\partial^2 (G^{Liq}/RT)}{\partial X_{\text{Al}} \partial X_{\text{Zr}}} & \frac{\partial^2 (G^{Liq}/RT)}{\partial X_{\text{Al}}^2} & \frac{\partial^2 (G^{Liq}/RT)}{\partial X_{\text{Al}} \partial X_{\text{Y}}} \\ \frac{\partial^2 (G^{Liq}/RT)}{\partial X_{\text{Y}} \partial X_{\text{Zr}}} & \frac{\partial^2 (G^{Liq}/RT)}{\partial X_{\text{Al}} \partial X_{\text{Y}}} & \frac{\partial^2 (G^{Liq}/RT)}{\partial X_{\text{Y}}^2} \end{vmatrix} \quad (6)$$

Table 1
Thermodynamic parameters of the Cu-Zr-Al-Y system for liquid phase.

Binary pair	Thermodynamic parameters for liquid phase	Ref.
Cu-Y	${}^0L_{Cu,Y}^{Liq} = -113556.81 + 142.61488 T - 16.755657 T \ln T$	[60]
	${}^1L_{Cu,Y}^{Liq} = -30872.77 - 17.50398 T$	
	${}^2L_{Cu,Y}^{Liq} = -317.55$	
	${}^3L_{Cu,Y}^{Liq} = +2882.66$	
Cu-Zr	${}^0L_{Cu,Zr}^{Liq} = -59880 - 8.940 T$	[61]
	${}^1L_{Cu,Zr}^{Liq} = +2987 + 3.391 T$	
	${}^2L_{Cu,Zr}^{Liq} = +6303 + 9.401 T$	
Al-Cu	${}^0L_{Al,Cu}^{Liq} = -67094 + 8.555 T$	[62]
	${}^1L_{Al,Cu}^{Liq} = +32148 - 7.118 T$	
	${}^2L_{Al,Cu}^{Liq} = +5915 - 5.889 T$	
	${}^3L_{Al,Cu}^{Liq} = -8175 + 6.049 T$	
Al-Zr	${}^0L_{Al,Zr}^{Liq} = -207140 + 42.911 T$	[63]
	${}^1L_{Al,Zr}^{Liq} = -22643 + 11.442 T$	
	${}^2L_{Al,Zr}^{Liq} = +56610 - 7.807 T$	
Al-Y	${}^0L_{Al,Y}^{Liq} = -192571.2 + 29.03622 T$	[64]
	${}^1L_{Al,Y}^{Liq} = -46742.9 - 0.46159 T$	
	${}^2L_{Al,Y}^{Liq} = +70259.0 - 28.99990 T$	
	${}^3L_{Al,Y}^{Liq} = +9002.8$	
Y-Zr	${}^0L_{Y,Zr}^{Liq} = +23902.39 + 0.09999 T$	[65]
	${}^1L_{Y,Zr}^{Liq} = +3000.29996$	

A negative value of the stability function indicates a thermodynamically unstable state of the alloy system and the corresponding compositions are inside the spinodal decomposition region. The critical compositional border for spinodal decomposition can be derived from the alloy compositions where $\varphi = 0$.

The miscibility gap calculated for the pseudo-binary section between the $Cu_{46}Zr_{47}Al_7$ and $Cu_{46}Y_{47}Al_7$ compositions is shown in Fig. 12(a). The horizontal axis of the pseudo-binary miscibility gap represents the yttrium content, i.e. the x value in $Cu_{46}Zr_{47-x}Al_7Y_x$ in atomic percent. Black and blue solid lines show the binodal and spinodal lines, respectively. The binodal line represents the thermodynamic critical temperatures (T_c) for phase separation depending on alloy composition. A general miscibility gap of a binary alloy system contains information for both T_c for phase

separation and equilibrium compositions of separated phases (= tie lines). However, a pseudo-binary miscibility gap of a multicomponent system, such as discussed in Fig. 12(a), is an expression of a partial section through an immiscible region in the n -dimensional thermodynamic space (compositions of $n-1$ elements + temperature), where n is the number of elements in the multicomponent system. The two-dimensional pseudo-binary miscibility gap can provide only information about T_c , and cannot describe the equilibrium compositions of the separated phases depending on the temperature where phase separation takes place. The tie lines between the equilibrium compositions in the Cu-Zr-Al-Y quaternary system can be described as exemplified in Fig. 12(b). The quaternary phase diagram section at $T = 600$ K shows the tie lines (colored solid lines with circular ends) depending on alloy composition (gray circles). The estimated tie lines reveal a phase separation trend between a more Zr-Al-rich phase (Liquid 1) on the one hand and a more Y-Cu-rich phase (Liquid 2) on the other hand. These compositional trends for the two phases match the APT results shown in terms of proxigrams in Fig. 6(b).

If an alloy melt enters the immiscible region in a supercooled liquid state, the melt can separate into two metastable liquid phases, which then solidify into two separate amorphous phases upon quenching. On the contrary, if the melt solidifies first into an amorphous state at a temperature above T_c , phase separation at short time scales during quenching is obviously kinetically hampered, due to the limited diffusivities of the elements in the solid state. The glass transition temperature (T_g) of a single liquid state (before phase separation) can be estimated by extrapolation from T_g s for alloys Y0, Y2 and Y5 measured by DSC (Fig. 1). These values are shown in terms of gray data points and a dotted line in Fig. 12(a). The relation between the T_g line and the miscibility gap reveals that the alloy Y10 and the corresponding alloys with lower Y content solidify before entering the immiscible region while the alloy Y15 and the alloys with higher Y content do not. This results in the observed differences of compositionally heterogeneous microstructures between the alloys Y10 and Y15. For the alloy Y15, phase separation takes place before vitrification to the amorphous solid phase and thus compositionally stable phases with sharp interfaces are formed. In contrast, the alloy Y10 does not undergo thermodynamic phase separation before vitrification but instead local clustering of Zr and Y atoms occurs even at temperature above the miscibility gap [68] due to their repulsive interaction. Analogous to pre-nucleation clusters [69] observed in the homogeneous region of phase diagrams, the chemical fluctuation in the alloy Y10 has no clear boundary between Y-rich and Zr-rich regions.

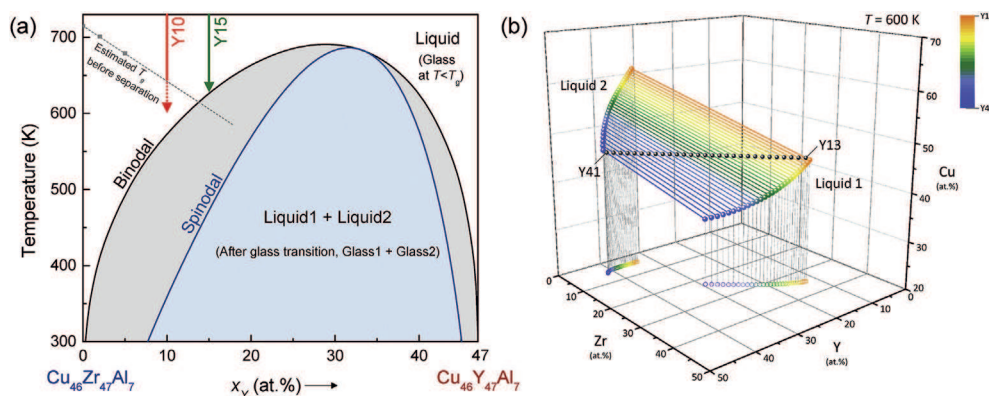


Fig. 12. (a) Calculated metastable miscibility gap for the liquid phase in Cu-Zr-Al-Y alloy system at pseudo-binary section between $Cu_{46}Zr_{47}Al_7$ and $Cu_{46}Y_{47}Al_7$ compositions. The dashed gray line shows the variation of glass transition temperature (T_g) as a function of overall composition, estimated from DSC traces in Fig. 1. (b) Tie lines depending on original alloy compositions of $Cu_{46}Zr_{47-x}Al_7Y_x$ alloys at a separation temperature of 600 K.

However, the pre-nucleation clusters are particle-like solute clusters associated with actual cluster size distributions in equilibrium [69], while the chemical fluctuation of the quaternary alloy forms rather spinodal-like bi-continuous networks of Y-rich and Zr-rich regions as observed in the APT reconstructions in Fig. 4(c).

The Landau-Lifshitz fluctuation theory [70] suggests a mean squared composition deviation of fluctuations following the relation $(\Delta C)^2 \propto (G'' + K\nabla C^2)^{-1}$ [68], where G'' is the curvature (= second derivative) of the molar free energy with respect to alloy composition, K is a gradient energy coefficient and ∇C is the spatial derivative of composition. At high temperatures far above T_c , G'' assumes a large value which induces thermally random motions of the elements, resulting in a homogeneous distribution. If the temperature approaches T_c , G'' becomes sufficiently small, causing large compositional fluctuations which continue to appear and decay temporally [68]. Thus, the amplitude of chemical fluctuations frozen during quenching depends significantly on the gap between T_c and T_g (Fig. 12(a)), as indeed observed for the difference between the results obtained for the alloys Y5 (< 1 nm) and Y10 (~ 4 nm).

4.2. Shear avalanches and plastic deformation behavior influenced by compositional heterogeneity in Cu-Zr-Al-Y as-spun ribbons

Statistical analysis of shear avalanches in metallic glasses, a phenomenon analogous to slip avalanches in crystalline materials [71], has been suggested as an important feature characterizing the plastic deformation of these materials, rendering it a suited object of investigation [50,72,73]. The shear avalanches in metallic glasses are spatiotemporal events emerging by elastically coupled STZs [73]. These intermittent and abrupt events are manifested as strain bursts when samples are exposed to load-controlled testing conditions (or as stress drops when probed in displacement-controlled mode). These sudden shear events carry and represent the amount of released elastic energy by momentary shear deformations. For some selected alloy samples (Y0, Y5, Y10 and Y15), the strain burst size distributions depending on alloy compositions (Fig. 8) have been converted into cumulative probability distribution functions, $P(>S)$, as shown in Fig. 13. The cumulative probability distribution of released elastic energy per pop-in event can be predicted by a universal power-law relationship [74,75] according to

$$P(>S) = AS^{-\beta} \exp\left(- (S/S_c)^2\right) \quad (7)$$

where A is a normalization constant, β is a scaling component which represents the slope of a log-log plot in the power law-scaling region ($S < S_c$), and S_c is the cut-off value of S where an

exponentially decaying behavior begins out of the power law relation. Using a Levenberg–Marquardt algorithm, $P(>S)$ for the four alloys were fitted by eq. (7) to estimate the parameters β and S_c . The fitting curves and resultant parameters are shown as solid lines in Fig. 13(a) and values in Fig. 13(b), respectively.

The parameters β and S_c reflect the size distribution profile of shear avalanches and the characteristic shear avalanche in metallic glasses, respectively [71,75]. A larger value of β indicates a sharper drop of $P(>S)$ with increasing S , which is equivalent to the relatively large population of small-sized strain burst events. Vice versa, a smaller value of β means a wider distribution of strain burst sizes that are not concentrated in a small S range. The relationship between β and the size distribution profile can be understood in terms of a comparison between the histograms (Fig. 8) and β values (Fig. 13(b)) of the alloys. The alloys Y10 and Y15 are characterized by a distribution of S that is largely concentrated within a small S range. They show drastically increased β values compared to the alloys Y0 and Y5. The distribution of S at $S < S_c$ (Stage I) follows a power-law distribution, ascribed to self-organized critical behavior in the occurrence of shear deformation [50,76]. In nanoindentation tests, a small strain burst can occur by a local activation of shear deformation units without forming a shear band along a viable plane when the local stress approaches the intrinsic strength [47]. The relatively small-sized shear avalanches in Stage I are interpreted in terms of the operation of the deformation mechanisms that carry plasticity, viz. STZs [2] or concordant shear-deformed regions [77], which remained in a jamming state [50,78,79]. At $S > S_c$ (Stage II), in contrast, an exponential decay of $P(>S)$ comes from large elastic strain fields overcoming the rigid jammed state of the deformation units and the associated emergence of chaotic shear avalanches [48]. The large shear avalanches in a chaotic state in Stage II lead to the nucleation and propagation of mature shear bands from the spatial connection of the deformation units. The characteristic strain burst size, S_c , is known to play a critical role in the rupture process of crystalline materials [71,80,81], but represents the susceptibility of chaotic shear band formation from the accumulated concordant regions jammed in Stage I for the case of metallic glasses.

Through the compositional change from Y0 to Y5, a slight increase of β and relatively large decrease of S_c indicate a reduction in the barrier for the formation of chaotic shear bands with a minor increase of population at $S < S_c$. This leads to the decrease of the critical stress for shear band nucleation without a significant change in sliding behaviors along the shear bands, as observed by strain bursts in micropillar compression test results (Fig. 9). However, the drastic increase of β in the alloys Y10 and Y15 compared to

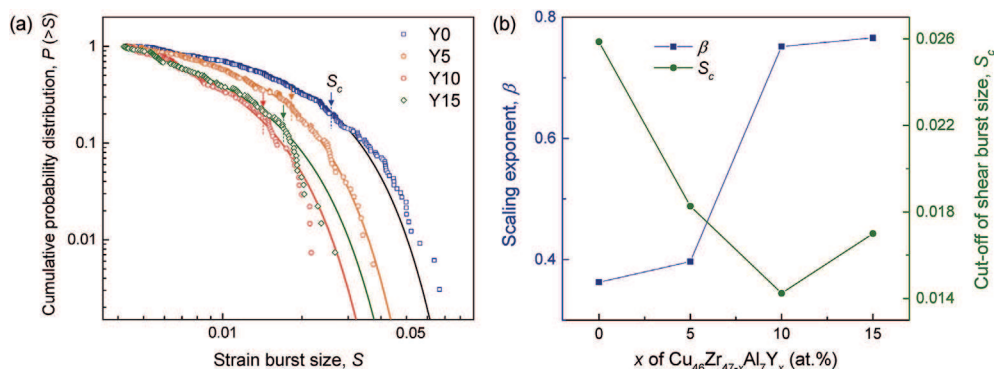


Fig. 13. Statistical analysis of shear avalanches in the series of nanoindentation results for as-spun $\text{Cu}_{46}\text{Zr}_{47-x}\text{Al}_7\text{Y}_x$ ($x = 0, 5, 10, 15$) alloy ribbons. (a) Cumulative probability distributions of strain burst size. Hollow data points represent experimental results collected from the nanoindentation results, and solid lines are fitting curves by Eq. (7). The arrows with dashed lines show the position of cut-off (S_c) values. (b) Variation of fitting parameters (S_c and β) as a function of Y composition in the Cu-Zr-Al-Y alloy ribbons.

the alloys Y0 and Y5 indicates that the small strain bursts related to jammed concordant regions are enormously promoted by a few-nm scale compositional heterogeneities. This can be attributed to the fact that the softer Y-rich region (or phase) acts as soft spots [17] preferred for the activation of shear deformation units. This effect is related to simulation results which indicate that metallic glasses can be toughened by introducing statistical heterogeneity of free volume without structural discontinuity [82,83]. The shear deformation is forced to activate locally at the chemically-induced soft spots of a few-nm scale by the surrounding rigid Zr-rich regions. The lower S_c values of the alloys Y10 and Y15 compared to that of the alloy Y0 also indicate easier nucleation of chaotic shear bands, which is supported by the concordant regions enormously accumulated at Stage I in contrast to the alloy Y5. This results in the multiple nucleation of shear bands with random directions as observed in Fig. 10(c,d), and sluggish deformation behavior along the shear bands (Fig. 9) due to the simultaneous operation of shear deformation in relatively large volumes, i.e. in a large total volume comprised of all the activated shear bands.

In order to compare shear band sliding behaviors with respect to alloy compositions, the viscosity (η) inside shear bands activated during micropillar tests is estimated by $\eta = \tau_s / \dot{\gamma}$, where the shear stress is $\tau_s = \sigma \sin\theta \cos\theta$ [84], the shear strain $\gamma = (\Delta\epsilon H) / (h \cos\theta)$ [75] and the shear strain rate $\dot{\gamma} = d\gamma/dt$. H is the height of the micropillar, and h is the thickness of shear bands assumed to be ~ 10 nm in extension [85]. The shear banding angle θ is measured from the morphology of compressed pillars to be approximately 43° . The minimum value of viscosity during a single strain burst (η_{Min}) is estimated in each strain burst event, and the average value of $\log_{10}(\eta_{Min})$ is presented for various alloy compositions in Fig. 14. The alloys Y0 and Y5 have a similar range of shear band viscosity during the strain burst, which reveals no significant difference in the nature of the shear bands between the two alloys. On the other hand, the viscosity elevates to a higher range with increasing Y content toward the alloys Y10 and Y15 by the activation of multiple shear bands (i.e. a larger shear band volume contributing to the sliding event associated with a single pop-in). The higher S_c value of the alloy Y15 compared to the alloy Y10 indicates the larger amount

of accumulated concordant regions before the onset of chaotic shear banding, which leads to the sluggish behavior of shear bands with slightly higher viscosity in the alloy Y15 compared to the alloy Y10.

We showed here that phase interfaces formed by phase separation inside a miscibility gap significantly affect the plastic flow stress of Cu-Zr-Al-Y metallic glasses. The $\text{Cu}_{46}\text{Zr}_{47-x}\text{Al}_7\text{Y}_x$ alloys with $x \geq 15$ at.% show a clear separation between a Zr-rich amorphous phase and a Y-rich amorphous phase with sharp interfaces, while alloys with $x \leq 10$ at.% have continuous compositional fluctuations without a clear interface between the Zr-rich and the Y-rich regions. Alloys without separated phases are characterized by a consecutive decrease of σ_f with increasing Y content and intensified compositional fluctuations. Alloys with phase interfaces exhibit σ_f values at a constant level (Fig. 11). A comparable trend is also found in the variation of the hardness as a function of alloy composition (Fig. 7). The hardness of those alloys containing phase interfaces shows obviously large but consistent deviations from the theoretical hardness estimated by the rule of mixtures compared to alloys that are devoid of interfaces. These results suggest that the phase interfaces play indeed a critical role in the stress level required for the onset of plastic deformation of PS-MGs by acting as a preferred path for rapid propagation of shear bands after their nucleation. For example, even though the separate phases sized only a few-nm in the alloy Y15 induce the multiple nucleation of randomly distributed shear bands, their interface provokes relatively rapid propagation of the shear bands at a low flow stress. However, the compositional fluctuation of ultrafine-scale below a few nm without the presence of interfaces can promote the multiple nucleation of shear bands with minimizing the loss of resistance against shear band propagation and the sluggish deformation along shear bands, as demonstrated by the alloy Y10.

5. Conclusions

The compositionally heterogeneous microstructures in $\text{Cu}_{46}\text{Zr}_{47-x}\text{Al}_7\text{Y}_x$ metallic glasses were confirmed by the combination of SANS and APT analysis. Based on the thermodynamic assessment of a metastable miscibility gap in the alloy system, we confirmed that continuous chemical fluctuations without distinct interfaces can be introduced at the outside of the miscibility gap where $x \leq 10$ at.% and $T > T_c$, while nanoscale phase separation takes place before vitrification inside the miscibility gap where $x \geq 15$ at.%. As a result, alloys with $x \leq 10$ at.% form a monolithic metallic glass with ultrafine compositional fluctuations while alloys with $x \geq 15$ at.% solidify into metallic glass composites consisting of dual amorphous phases. Especially, the alloy Y10 forms a monolithic metallic glass that has a few-nm scale compositional fluctuations with a spinodal-like network structure, while the alloy Y15 vitrifies into two nanoscale amorphous phases with sharp phase-interfaces. The statistical analysis of shear avalanches occurring during nanoindentation tests of the alloys reveals that the compositional heterogeneities in a few-nm scale in the alloys Y10 and Y15 may act as chemically-induced soft spots for preferentially accommodating shear deformation. This results in not only the multiple nucleation of shear bands in various random directions but also the sluggish deformation behavior along the shear bands in micropillar compression tests. However, hardness measurements and bending test results demonstrate that the presence of phase interfaces in alloys with $x \geq 15$ at.% deteriorates the resistance against shear band propagation. This drawback can be avoided by controlling the nanoscale chemical heterogeneities into a continuously fluctuating state without the presence of distinct interfaces as introduced in the alloy Y10. These results suggest an effective strategy for modulating shear avalanches and enhancing the

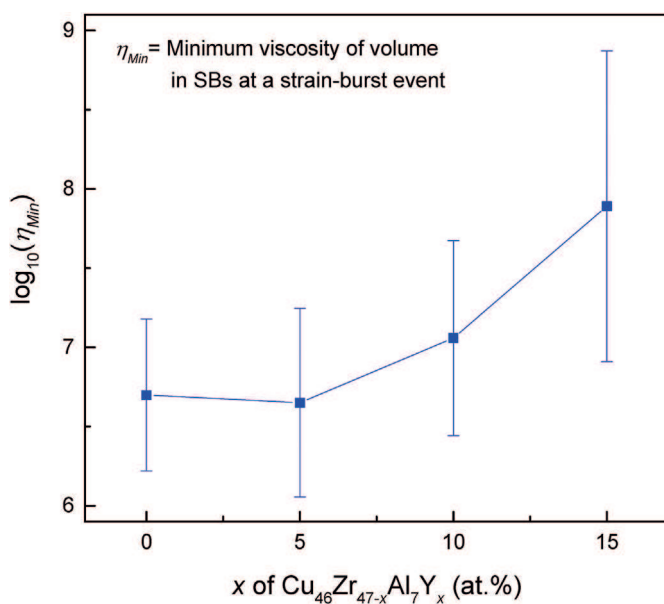


Fig. 14. Averaged minimum viscosity (η_{Min}) of the volume in shear bands at a strain-burst event in compressed $\text{Cu}_{46}\text{Zr}_{47-x}\text{Al}_7\text{Y}_x$ ($x = 0, 5, 10, 15$) micropillars. The standard deviations of estimated values were taken as the error values.

plasticity of metallic glasses via nanoscale networks of compositional heterogeneities arising from the relationship between T_C and T_g , which can be eventually connected with bulk forms by considering kinetic aspects for compositional fluctuation during vitrification.

Acknowledgements

This work was supported by the National Research Foundation of Korea grant funded by the Korean government (Ministry of Science, ICT and Future Planning) (No. NRF-2014K1A3A1A20034841). The SANS experiments were performed at High flux Advanced Neutron Application Reactor (HANARO) 40 m SANS beam line supported by Korea Atomic Energy Research Institute (KAERI) (Proposal No. NB-40MSANS/2013-0038, NB-40MSANS/2012-0115). We thank Dr. Mathias Köhler for helping APT experiments.

Appendix A. Supplementary data

Supplementary data related to this article can be found at <http://dx.doi.org/10.1016/j.actamat.2017.08.002>.

References

- [1] A.L. Greer, *Metallic glasses*, Science 267 (1995) 1947–1953.
- [2] A.S. Argon, Plastic deformation in metallic glasses, *Acta Metall.* 27 (1979) 47–58.
- [3] P.S. Steif, F. Spaepen, J.W. Hutchinson, Strain localization in amorphous metals, *Acta Metall.* 30 (1982) 447–455.
- [4] C.A. Schuh, T.C. Hufnagel, U. Ramamurty, Mechanical behavior of amorphous alloys, *Acta Mater.* 55 (2007) 4067–4109.
- [5] D.C. Hofmann, J.-Y. Suh, A. Wiest, G. Duan, M.-L. Lind, M.D. Demetriou, W.L. Johnson, Designing metallic glass matrix composites with high toughness and tensile ductility, *Nature* 451 (2008) 1085–1089.
- [6] S. Pauly, S. Gorantla, G. Wang, U. Kühn, J. Eckert, Transformation-mediated ductility in CuZr-based bulk metallic glasses, *Nat. Mater.* 9 (2010) 473–477.
- [7] Y. Wu, Y. Xiao, G. Chen, C.T. Liu, Z. Lu, Bulk metallic glass composites with transformation-mediated work-hardening and ductility, *Adv. Mater.* 22 (2010) 2770–2773.
- [8] R.L. Narayan, P.S. Singh, D.C. Hofmann, N. Hutchinson, K.M. Flores, U. Ramamurty, On the microstructure–tensile property correlations in bulk metallic glass matrix composites with crystalline dendrites, *Acta Mater.* 60 (2012) 5089–5100.
- [9] J. Qiao, H. Jia, P.K. Liaw, Metallic glass matrix composites, *Mater. Sci. Eng. R.* 100 (2016) 1–69.
- [10] Y. Sun, A. Concustell, A.L. Greer, Thermomechanical processing of metallic glasses: extending the range of the glassy state, *Nat. Rev. Mater.* 1 (2016) 16039.
- [11] D.H. Kim, W.T. Kim, E.S. Park, N. Mattern, J. Eckert, Phase separation in metallic glasses, *Prog. Mater. Sci.* 58 (2013) 1103–1172.
- [12] S.V. Ketov, Y.H. Sun, S. Nachum, Z. Lu, A. Checchi, A.R. Beraldin, H.Y. Bai, W.H. Wang, D.V. Louzguine-Luzgin, M.A. Carpenter, A.L. Greer, Rejuvenation of metallic glasses by non-affine thermal strain, *Nature* 524 (2015) 200–203.
- [13] H.B. Ke, P. Wen, H.L. Peng, W.H. Wang, A.L. Greer, Homogeneous deformation of metallic glass at room temperature reveals large dilatation, *Scr. Mater.* 64 (2011) 966–969.
- [14] K.-W. Park, C.-M. Lee, M. Wakeda, Y. Shibutani, M.L. Falk, J.-C. Lee, Elastostatically induced structural disordering in amorphous alloys, *Acta Mater.* 56 (2008) 5440–5450.
- [15] F. Meng, K. Tsuchiya, Seiichiro II, Y. Yokoyama, Reversible transition of deformation mode by structural rejuvenation and relaxation in bulk metallic glass, *Appl. Phys. Lett.* 101 (2012) 121914.
- [16] Y. Zhang, W.H. Wang, A.L. Greer, Making metallic glasses plastic by control of residual stress, *Nat. Mater.* 5 (2006) 857–860.
- [17] J. Ding, S. Patinet, M.L. Falk, Y. Cheng, E. Ma, Soft spots and their structural signature in a metallic glass, *Proc. Natl. Acad. Sci.* 111 (2014) 14052–14056.
- [18] E.S. Park, D.H. Kim, Phase separation and enhancement of plasticity in Cu–Zr–Al–Y bulk metallic glasses, *Acta Mater.* 54 (2006) 2597–2604.
- [19] E.S. Park, J.S. Kyeong, D.H. Kim, Phase separation and improved plasticity by modulated heterogeneity in Cu–(Zr, Hf)–(Gd, Y)–Al metallic glasses, *Scr. Mater.* 57 (2007) 49–52.
- [20] L.Q. Xing, Y. Li, K.T. Ramesh, J. Li, T.C. Hufnagel, Enhanced plastic strain in Zr-based bulk amorphous alloys, *Phys. Rev. B* 64 (2001) 180201.
- [21] M.H. Lee, J.Y. Lee, D.H. Bae, W.T. Kim, D.J. Sordelet, D.H. Kim, A development of Ni-based alloys with enhanced plasticity, *Intermetallics* 12 (2004) 1133–1137.
- [22] E.S. Park, D.H. Kim, T. Ohkubo, K. Hono, Enhancement of glass forming ability and plasticity by addition of Nb in Cu–Ti–Zr–Ni–Si bulk metallic glasses, *J. Non-Cryst. Solids* 351 (2005) 1232–1238.
- [23] E.S. Park, H.J. Chang, D.H. Kim, T. Ohkubo, K. Hono, Effect of the substitution of Ag and Ni for Cu on the glass forming ability and plasticity of Cu60Zr30Ti10 alloy, *Scr. Mater.* 54 (2006) 1569–1573.
- [24] A.I. Takeuchi, Akihisa, Classification of bulk metallic glasses by atomic size difference, heat of mixing and period of constituent elements and its application to characterization of the main alloying element, *Mater. Trans.* 46 (2005) 2817–2829.
- [25] A.A. Kündig, M. Ohnuma, D.H. Ping, T. Ohkubo, K. Hono, In situ formed two-phase metallic glass with surface fractal microstructure, *Acta Mater.* 52 (2004) 2441–2448.
- [26] B.J. Park, H.J. Chang, D.H. Kim, W.T. Kim, K. Chattopadhyay, T.A. Abinandanan, S. Bhattacharyya, Phase separating bulk metallic glass: a hierarchical composite, *Phys. Rev. Lett.* 96 (2006) 245503.
- [27] H.J. Chang, W. Yook, E.S. Park, J.S. Kyeong, D.H. Kim, Synthesis of metallic glass composites using phase separation phenomena, *Acta Mater.* 58 (2010) 2483–2491.
- [28] J.H. Han, N. Mattern, B. Schwarz, D.H. Kim, J. Eckert, Phase separation and magnetic properties in Gd–(Hf,Ti,Y)–Co–Al metallic glasses, *Scr. Mater.* 67 (2012) 149–152.
- [29] J.H. Han, N. Mattern, D.H. Kim, J. Eckert, Phase separation and microstructure evolution of rapidly quenched Gd–Hf–Co–Al alloys, *J. Alloy Compd.* 509 (1) (2011) S42–S45.
- [30] N. Mattern, T. Gemming, J. Thomas, G. Goerigk, H. Franz, J. Eckert, Phase separation in Ni–Nb–Y metallic glasses, *J. Alloy Compd.* 495 (2010) 299–304.
- [31] S.W. Sohn, W. Yook, W.T. Kim, D.H. Kim, Phase separation in bulk-type Gd–Zr–Al–Ni metallic glass, *Intermetallics* 23 (2012) 57–62.
- [32] A.A. Kündig, T. Schweizer, E. Schafner, J.F. Löffler, Metallic glass/polymer composites by co-processing at similar viscosities, *Scr. Mater.* 56 (2007) 289–292.
- [33] Y.-S. Han, S.-M. Choi, T.-H. Kim, C.-H. Lee, H.-R. Kim, Design of 40M SANS instrument at HANARO, Korea, *Phys. B Condens. Matter.* 385–386, Part 2 (2006) 1177–1179.
- [34] K. Thompson, D. Lawrence, D.J. Larson, J.D. Olson, T.F. Kelly, B. Gorman, In situ site-specific specimen preparation for atom probe tomography, *Ultra-microscopy* 107 (2007) 131–139.
- [35] M.K. Miller, *Atom Probe Tomography: Analysis at the Atomic Level*, Kluwer Academic/Plenum Publishers, New York, 2000.
- [36] M.P. Moody, L.T. Stephenson, A.V. Ceguerra, S.P. Ringer, Quantitative binomial distribution analyses of nanoscale like-solute atom clustering and segregation in atom probe tomography data, *Microsc. Res. Tech.* 71 (2008) 542–550.
- [37] H.J. Chang, E.S. Park, Y.C. Kim, D.H. Kim, Observation of artifact-free amorphous structure in Cu–Zr-based alloy using transmission electron microscopy, *Mater. Sci. Eng. A* 406 (2005) 119–124.
- [38] T.T. Sasaki, T. Ohkubo, K. Hono, Y. Une, M. Sagawa, Correlative multi-scale characterization of a fine grained Nd–Fe–B sintered magnet, *Ultra-microscopy* 132 (2013) 222–226.
- [39] H. Jaksch, J.P. Vermeulen, New developments in GEMINI®FESEM technology, *Microsc. Today* 13 (2005) 8–10.
- [40] G. Beaucage, Approximations leading to a unified exponential/power-law approach to small-angle scattering, *J. Appl. Crystallogr.* 28 (1995) 717–728.
- [41] J. Ilavsky, P.R. Jemian, Irena: tool suite for modeling and analysis of small-angle scattering, *J. Appl. Crystallogr.* 42 (2009) 347–353.
- [42] A. Guinier, La diffraction des rayons X aux très petits angles; application à l'étude de phénomènes ultramicroscopiques, *Ann. Phys.* 12 (1939) 161–237.
- [43] O.C. Hellman, J.A. Vandenbroucke, J. Rüsing, D. Isheim, D.N. Seidman, Analysis of three-dimensional atom-probe data by the proximity histogram, *Microsc. Microanal.* 6 (2000) 437–444.
- [44] W. Voigt, Ueber die Beziehung zwischen den beiden Elastizitätsconstanten isotroper Körper, *Wied. Ann.* 274 (1889) 573–587.
- [45] A. Reuss, Berechnung der Fließgrenze von Mischkristallen auf Grund der Plastizitätsbedingung für Einkristalle, *Z. Angew. Math. Mech.* 9 (1929) 49–58.
- [46] H.S. Kim, On the rule of mixtures for the hardness of particle reinforced composites, *Mater. Sci. Eng. A* 289 (2000) 30–33.
- [47] Y.Q. Cheng, E. Ma, Intrinsic shear strength of metallic glass, *Acta Mater.* 59 (2011) 1800–1807.
- [48] B.A. Sun, H.B. Yu, W. Jiao, H.Y. Bai, D.Q. Zhao, W.H. Wang, Plasticity of ductile metallic glasses: a self-organized critical state, *Phys. Rev. Lett.* 105 (2010) 035501.
- [49] J.I. Lee, J.W. Kim, H.S. Oh, J.S. Park, E.S. Park, Abnormal devitrification behavior and mechanical response of cold-rolled Mg-rich Mg–Cu–Gd metallic glasses, *Acta Mater.* 116 (2016) 238–249.
- [50] X.L. Bian, G. Wang, K.C. Chan, J.L. Ren, Y.L. Gao, Q.J. Zhai, Shear avalanches in metallic glasses under nanoindentation: deformation units and rate dependent strain burst cut-off, *Appl. Phys. Lett.* 103 (2013) 101907.
- [51] C.A. Volkert, A. Donohue, F. Spaepen, Effect of sample size on deformation in amorphous metals, *J. Appl. Phys.* 103 (2008) 083539.
- [52] Y.H. Lai, C.J. Lee, Y.T. Cheng, H.S. Chou, H.M. Chen, X.H. Du, C.I. Chang, J.C. Huang, S.R. Jian, J.S.C. Jang, T.G. Nieh, Bulk and microscale compressive behavior of a Zr-based metallic glass, *Scr. Mater.* 58 (2008) 890–893.
- [53] B.E. Schuster, Q. Wei, T.C. Hufnagel, K.T. Ramesh, Size-independent strength and deformation mode in compression of a Pd-based metallic glass, *Acta Mater.* 56 (2008) 5091–5100.
- [54] E.P. Barth, F. Spaepen, R. Bye, S.K. Das, Influence of processing on the ductile-

- to-brittle transition temperature of an Fe-B-Si metallic glass, *Acta Mater.* 45 (1997) 423–428.
- [55] D.G. Ast, D.J. Krenitsky, Evidence for ideal elastic-plastic deformation in Fe-Ni-based metallic glasses, *Mater. Sci. Eng.* 43 (1980) 241–246.
- [56] W.C. Oliver, G.M. Pharr, An improved technique for determining hardness and elastic modulus using load and displacement sensing indentation experiments, *J. Mater. Res.* 7 (1992) 1564–1583.
- [57] G. Simmons, H. Wang, *Single Crystal Elastic Constants and Calculated Aggregate Properties: A Handbook*, Mass., M.I.T. Press, Cambridge, 1971.
- [58] P. Yu, H.Y. Bai, W.H. Wang, Superior glass-forming ability of CuZr alloys from minor additions, *J. Mater. Res.* 21 (2006) 1674–1679.
- [59] W.H. Wang, The elastic properties, elastic models and elastic perspectives of metallic glasses, *Prog. Mater. Sci.* 57 (2012) 487–656.
- [60] O. Redlich, A.T. Kister, Algebraic representation of thermodynamic properties and the classification of solutions, *Industrial Eng. Chem.* 40 (1948) 345–348.
- [61] U. Abend, H.J. Schaller, Constitution and thermodynamics of Cu-Y alloys, *Ber. Bunsenges. Phys. Chem.* 101 (1997) 741–748.
- [62] K. Yamaguchi, Y.-C. Song, T. Yoshida, K. Itagaki, Thermodynamic investigation of the Cu–Zr system, *J. Alloy Compd.* 452 (2008) 73–79.
- [63] V.T. Witusiewicz, U. Hecht, S.G. Fries, S. Rex, The Ag–Al–Cu system: Part I: reassessment of the constituent binaries on the basis of new experimental data, *J. Alloy Compd.* 385 (2004) 133–143.
- [64] T. Wang, Z. Jin, J.-C. Zhao, Thermodynamic assessment of the Al–Zr binary system, *J. Phase Equil* 22 (2001) 544–551.
- [65] S. Liu, Y. Du, H. Chen, A thermodynamic reassessment of the Al–Y system, *Calphad* 30 (2006) 334–340.
- [66] X.C. He, H.S. Liu, Determination of the isothermal section of the Cu–Zr–Y ternary system at 978 K, *J. Alloy Compd.* 475 (2009) 245–251.
- [67] C.H.P. Lupis, *Chemical Thermodynamics of Materials*, North-Holland, 1983.
- [68] P.P. Camus, Atom probe analysis of solute clustering above a miscibility gap, *J. Phys. Colloq.* 48 (1987). C6-331–C6-336.
- [69] D. Gebauer, M. Kellermeier, J.D. Gale, L. Bergstrom, H. Colfen, Pre-nucleation clusters as solute precursors in crystallisation, *Chem. Soc. Rev.* 43 (2014) 2348–2371.
- [70] L.D. Landau, E.M. Lifshitz, *Statistical Physics*, Elsevier Science, 2013.
- [71] T. Richeton, J. Weiss, F. Louchet, Breakdown of avalanche critical behaviour in polycrystalline plasticity, *Nat. Mater.* 4 (2005) 465–469.
- [72] K.A. Dahmen, Y. Ben-Zion, J.T. Uhl, Micromechanical model for deformation in solids with universal predictions for stress-strain curves and slip avalanches, *Phys. Rev. Lett.* 102 (2009) 175501.
- [73] J. Antonaglia, W.J. Wright, X. Gu, R.R. Byer, T.C. Hufnagel, M. LeBlanc, J.T. Uhl, K.A. Dahmen, Bulk metallic glasses deform via slip avalanches, *Phys. Rev. Lett.* 112 (2014) 155501.
- [74] J. Antonaglia, X. Xie, G. Schwarz, M. Wraith, J. Qiao, Y. Zhang, P.K. Liaw, J.T. Uhl, K.A. Dahmen, Tuned critical avalanche scaling in bulk metallic glasses, *Sci. Rep.* 4 (2014) 4382.
- [75] X. Tong, G. Wang, J. Yi, J.L. Ren, S. Pauly, Y.L. Gao, Q.J. Zhai, N. Mattern, K.A. Dahmen, P.K. Liaw, J. Eckert, Shear avalanches in plastic deformation of a metallic glass composite, *Int. J. Plast.* 77 (2016) 141–155.
- [76] P. Bak, C. Tang, K. Wiesenfeld, Self-organized criticality: an explanation of the 1/f noise, *Phys. Rev. Lett.* 59 (1987) 381–384.
- [77] G. Wang, N. Mattern, J. Bednarcik, R. Li, B. Zhang, J. Eckert, Correlation between elastic structural behavior and yield strength of metallic glasses, *Acta Mater.* 60 (2012) 3074–3083.
- [78] C.S. O'Hern, L.E. Silbert, A.J. Liu, S.R. Nagel, Jamming at zero temperature and zero applied stress: the epitome of disorder, *Phys. Rev. E* 68 (2003) 011306.
- [79] M. Wyart, S.R. Nagel, T.A. Witten, Geometric origin of excess low-frequency vibrational modes in weakly connected amorphous solids, *EPL Europhys. Lett.* 72 (2005) 486.
- [80] S. Papanikolaou, D.M. Dimiduk, W. Choi, J.P. Sethna, M.D. Uchic, C.F. Woodward, S. Zapperi, Quasi-periodic events in crystal plasticity and the self-organized avalanche oscillator, *Nature* 490 (2012) 517–521.
- [81] Z. Michael, M. Paolo, Fluctuation phenomena in crystal plasticity—a continuum model, *J. Stat. Mech. Theory. Exp.* 2005 (2005), P08004.
- [82] Y. Wang, M. Li, J. Xu, Toughen and harden metallic glass through designing statistical heterogeneity, *Scr. Mater.* 113 (2016) 10–13.
- [83] Y. Wang, M. Li, J. Xu, Mechanical properties of spinodal decomposed metallic glass composites, *Scr. Mater.* 135 (2017) 41–45.
- [84] S.X. Song, T.G. Nieh, Direct measurements of shear band propagation in metallic glasses – an overview, *Intermetallics* 19 (2011) 1968–1977.
- [85] Y. Zhang, A.L. Greer, Thickness of shear bands in metallic glasses, *Appl. Phys. Lett.* 89 (2006) 071907.